

Reduced Lagrange multiplier approach for the non-matching coupled problems in multiscale elasticity

Camilla Belponer^{1,2}, Alfonso Caiazzo², and Luca Heltai³

¹*Augsburg Universität, Universitätsstraße 2, 86159 Augsburg, Germany*

²*Weierstrass Institute for Applied Mathematics and Stochastics (WIAS), Mohrenstrasse 39, 10117 Berlin, Germany*

³*International School for Advanced Studies (SISSA), Via Bonomea 265, 34136, Trieste, TS, Italy*

September 15, 2023

Abstract

This paper presents a numerical method for the simulation of elastic solid materials coupled to fluid inclusions. The application is motivated by the modeling of vascularized tissues and by problems in medical imaging which target the estimation of effective (i.e., macroscale) material properties, taking into account the influence of microscale dynamics, such as fluid flow in the microvasculature. The method is based on the recently proposed Reduced Lagrange Multipliers framework. In particular, the interface between solid and fluid domains is not resolved within the computational mesh for the elastic material but discretized independently, imposing the coupling condition via non-matching Lagrange multipliers. Exploiting the multiscale properties of the problem, the resulting Lagrange multipliers space is reduced to a lower-dimensional characteristic set. We present the details of the stability analysis of the resulting method considering a non-standard boundary condition that enforces a local deformation on the solid-fluid boundary. The method is validated with several numerical examples.

Keywords: Finite element method; linear elasticity; multiscale methods; model reduction; immersed interfaces; Lagrange multipliers

1 Introduction

This paper focuses on the computational multiscale modeling of elastic materials whose dynamics depend on the interaction between an elastic matrix and slender fluid-filled inclusions. The research is motivated by applications in biological tissue imaging, such as multiparametric MRI with diffusion-weighted imaging [30, 35], or magnetic resonance elastography (MRE) [38, 41, 45, 44], where image data are combined with physical models of vascularized tissue to estimate material and mechanical tissue properties.

Fully resolved fluid-structure interaction models require the handling of multiple physics – the solid matrix and the fluid vasculature – and are prohibitive due to the geometrical complexity at the small scales (vascular structures) and by the need of handling the fluid-solid coupling. At the same time, in the context of medical images, data are typically available only at the macroscale (effective tissue, with a resolution of the order of millimeters), requiring the usage of suitable upscaled tissue models.

To bridge the gap between model complexity and available data resolution, tissue models based on linearized elasticity and poroelasticity are commonly used in the context of medical imaging to characterize mechanical and constitutive *effective* parameters. However, in selected contexts, it is necessary to use *multiscale* surrogate models, i.e., capable of retaining the details of the microscale vasculature, even if these are related to smaller spatial scales, not always resolved in the available data (e.g., the image resolution). An example is the possibility of characterizing the effect on macroscopic-biophysical parameters of the variations of the fluid pressure along the vascular network. A concrete example on the sensitivity of liver tissue parameters to intrinsic poroelastic properties and vascular architecture has been recently presented and discussed in the experimental study presented by Safraou et al. [46], investigating the influence of static portal pressure on liver stiffness (see also [39, 43]).

Multiscale methods based on homogenization and local orthogonal decomposition (see, e.g., [29, 4]) can provide suitable approaches to tackle this challenge both for forward problems (see, e.g., [6, 14, 21] for recent applications in the context of elasticity and poroelasticity) and inverse problems (see, e.g., [16, 22]). These frameworks can efficiently describe the dynamics across multiple scales, taking into account more general microstructure descriptions, and without requiring excessive assumptions on the microstructures neither their resolution at full scale. Instead, surrogate, effective, models are obtained by solving selected realizations of microscale problems (also called *cell problems*).

This work is devoted to the efficient modeling of such cell problems in the context of multiscale elasticity and fluid-structure interaction. We describe, analyze, and validate a numerical method in which a tissue sample is modeled as a linear elastic matrix coupled to an arbitrary vascular fluid structures of co-dimension two (i.e., 3D-1D or 2D-0D).

The fluid-solid coupling is handled using a non-matching immersed method. The

model is inspired by the approach recently presented in [26, 27], in which the coupling was implemented via a singular forcing term in the elasticity equation, imposing a Neumann-like boundary condition computed from an asymptotic approximation of a local analytical solution. We aim at extending this approach to more general boundary conditions. In particular, we consider a *local deformation* Dirichlet boundary condition for the elastic problem, in which the coupling between small fluid vessels and solid tissue does not depend on the solid deformation at the macroscale level. This local deformation is necessary to target applications in the context of homogenization, in order to have a cell problem that can simulate the microscale dynamics and does not depend, on a first approximation, on the larger scales.

To robustly enforce this non standard boundary condition, we extend the model proposed in [26, 27] using the *reduced* Lagrange multipliers framework recently described by Heltai & Zunino [28].

The Lagrange multipliers (LM) method [9, 13] plays an important role in the numerical solution of partial differential equations using the finite element method, in particular in the context of coupled multiphysics and multiscale models (see, e.g., [11, 12, 20] for some recent examples). In this approach the finite element formulation is defined based on a minimization problem equivalent to the original PDE, in which the boundary (or the coupling) conditions are imposed weakly as a set of constraints using functional spaces defined on the interfaces. The idea of mixed-dimensional methods is to reduce part of the physics on a lower-dimensional manifold on which the dynamics can be sufficiently well approximated. These models have been first analyzed in [19] in the context of diffusion, and later on applied also to perfusion, porous media flows [17, 18, 31], and elasticity (e.g., [26]). Recent LM formulations for mixed-dimensional material models were proposed, e.g., in [7], considering the coupling of a three-dimensional bulk mechanical problem with one-dimensional fiber structures. Preliminary stability results for Dirichlet-Neumann coupling conditions on mixed-dimensional (3D-1D) problems using LM were recently presented in [33], and suitable preconditioning strategies are discussed in [32, 15].

The reduced LM approach addresses the dimensional reduction of the functional space of Lagrange multipliers. Namely, under the assumption of slender (cylindrical) vessels with mostly one-dimensional dynamics, the centerline is considered as a representative lower dimensional manifold, and the dimension reduction is achieved by approximating the (infinite-dimensional) space of Lagrange multipliers on the two-dimensional vessel boundary with a collection of infinite dimensional Fourier modes on the one-dimensional center-line of the vessel.

Other alternatives for applying model-order reduction in the context of multiscale and mixed-dimensional modeling have been described, for example, in [1], in which a reduced-basis approach at the macroscale has been employed to reduce the number of required solutions at the microscale. The predominance of the one-dimensional dynamics was also exploited for the definition of a hierarchical model reduction [3, 37] to efficiently compute the flow in long pipes, reducing the dimensionality of the orthogonal

dimensions. A possible application of Localized Orthogonal Decomposition methods (LOD) to mixed-dimensional problems and to LM has been recently proposed in [5] for the coupling of bulk (2D) and surface (1D) problems, considering the numerical homogenization of the dynamics on the one-dimensional manifold and enforcing the resulting interface conditions with LM.

The contribution of this work is twofold. First, we extend of the approach of [28] to the case of multiscale elasticity. In particular, we show that the reduced Lagrange multipliers framework provides a natural way to handle the local deformation boundary condition and extend the stability analysis of [28] to this case. Focusing on the case of axis-symmetric boundary conditions (deformation along the normal direction) we discuss the reduced-order formulation from the theoretical and practical points of view and present detailed numerical validation in different examples. Next, we perform computational studies to discuss and investigate the implication of the proposed method for *in silico* tissue modeling, for the application in the context of numerical upscaling techniques, and for the solution of multiscale inverse problems for the estimation of tissue properties.

The rest of this paper is organized as follows. Section 2 introduces the main setting and the required notations, while Section 3 describes the considered mixed-dimensional elasticity problem. The reduced Lagrange multiplier formulation is introduced and analyzed in Section 4. The numerical results are presented and discussed in Sections 5, while Section 6 draws the concluding remarks.

2 Preliminaries

This section introduces the settings of the mixed-dimensional model, following the general framework recently introduced in [28] for dimensional reduction in coupled problem.

2.1 Multiscale setting

Let us consider a Lipschitz domain $\Omega \subseteq \mathbb{R}^d$, containing an elastic material and a set $V := \cup_{i=1}^m V_i$ of (possibly disconnected) fluid-filled inclusions V_i , $i = 1, \dots, m$. The boundary of the fluid domain will be denoted by $\Gamma := \partial V$. The proposed method is built on the following geometrical and physical assumptions.

Firstly, we assume that the inclusions are *slender*, i.e., that each V_i has two spatial dimensions along which the characteristic lengths are much smaller with respect to the remaining dimension. The set V can hence be approximated geometrically by subsets of co-dimension 2 (one-dimensional manifold in a three-dimensional problem, or an union of points for a two-dimensional case, see, e.g., the sketch in Figure 1).

Secondly, we assume that the fluid dynamics inside V can be described, with sufficient accuracy, considering a model on a lower-dimensional set γ with intrinsic dimension $d - 2$. We will refer to γ as the lower dimensional representative domain.

This setting is particularly relevant for the modeling of vascular tissues. In this case, V represents the physical space occupied by the fluid vessels and γ might represent a suitable one-dimensional representation of the vascular network, on which the fluid dynamics can be sufficiently well described by a one-dimensional flow model (see, e.g., [40]).

Thirdly, we introduce the following hypotheses on the structure of the inclusion (see also [28]).

Assumption 1 (Cylindrical vessels). *Each V_i , $i = 1, \dots, m$ can be written as the image of an isomorphism*

$$\hat{\Phi}_i : \hat{V} \rightarrow V_i,$$

where \hat{V} is a reference cylindrical inclusion domain with unit measure. Let $\hat{\gamma}_i$ be the preimages of the $d - 2$ lower-dimensional representative domains of each inclusion V_i , i.e., $\hat{\gamma}_i = \hat{\Phi}_i^{-1}(\gamma_i)$. We assume that each $\hat{\gamma}_i$ is a straight line directed along on the last coordinate axis in the three-dimensional case ($d = 3$) and it coincides with the origin in the two-dimensional case ($d = 2$).

Assumption 2 (Isomorphism). *The isomorphisms $\hat{\Phi}_i$, $i = 1, \dots, m$ satisfy the following hypotheses:*

- $\hat{\Phi}_i \in C^1(\hat{V})$, $\hat{\Phi}_i^{-1} \in C^1(V)$;
- there exist two positive constants J_{\min}, J_{\max} such that

$$0 < J_{\min} \leq \det(\nabla \hat{\Phi}_i(\hat{\mathbf{x}})) \leq J_{\max}, \quad \forall \hat{\mathbf{x}} \in \hat{V}.$$

Under the above Assumption 1, the boundary of the reference inclusion domain $\partial \hat{V}$ can be written as a tensor product of a circle times the $d - 2$ dimensional set $\hat{\gamma}$. The tensor product structure and the isomorphism can be used to define a geometrical projector operator

$$\Pi : \Gamma \rightarrow \gamma \tag{1}$$

that maps uniquely the inclusion boundary Γ onto the lower dimensional representative domain γ . The inverse of the projection, $\Pi^{-1} : \gamma \rightarrow \mathcal{P}(\Gamma)$, maps each point on γ on a suitable cross section of the vessel Γ . As in [28], let us denote with

$$D(s) := \Pi^{-1}(s) \tag{2}$$

the preimage of the projection operator, and define $dD(s) := d\mathcal{H}(\Pi^{-1}(s))$. For any $s \in \gamma$, let $|D(s)|$ denote for the intrinsic Hausdorff measure of the set $D(s)$.

Remark 1 (Example). *In the case of a single straight vessel V , denoting with γ its centerline, a suitable projection operator is the map that associates each cross-section $D(s)$, orthogonal to γ , to its center $s \in \gamma$.*

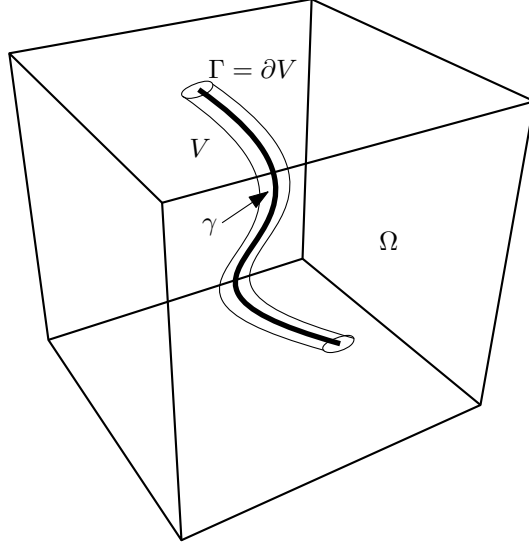


Figure 1: Sketch of 3D-1D dimensional reduction: a thin vessel is approximated by its centerline, and the fluid dynamics is modeled using one-dimensional Navier-Stokes equations.

We conclude this section introducing the following notations for standard Sobolev spaces:

$$\begin{aligned}
 \mathcal{V}_\Omega &\equiv H_0^1(\Omega)^d, & \mathcal{V}_\Omega' &\equiv H^{-1}(\Omega)^d, \\
 \mathcal{Q}_\Gamma &\equiv H^{-\frac{1}{2}}(\Gamma)^d, & \mathcal{Q}_\Gamma' &\equiv H^{\frac{1}{2}}(\Gamma)^d, \\
 \mathcal{W}_\gamma &\equiv H^{\frac{1}{2}}(\gamma)^d, & \mathcal{W}_\gamma' &\equiv H^{-\frac{1}{2}}(\gamma)^d,
 \end{aligned}$$

as well as the classical trace operator:

$$\mathcal{T} : \mathcal{V}_\Omega \mapsto \mathcal{Q}_\Gamma'. \quad (3)$$

2.2 Averaged trace operator

Let $\mathbf{f} : \Gamma \rightarrow \mathbb{R}^d$ be an absolutely integrable function on Γ . Following the definitions given in [28] for the scalar case, we define the operator

$$(\mathcal{A}^0 \mathbf{f})(s) := \frac{1}{|D(s)|} \int_{D(s)} \mathbf{f} \, dD(s) =: \left(\int_D \mathbf{f} \, dD \right) (s), \quad s \in \gamma. \quad (4)$$

which, for each $s \in \gamma$, computes the average of \mathbf{f} over the preimage $D(s)$.

Moreover, for any function $\mathbf{w} : \gamma \rightarrow \mathbb{R}^d$, we define the extension operator

$$(\mathcal{E}^0 \mathbf{w})(x) := (\mathbf{w} \circ \Pi)(x), \quad x \in \Gamma. \quad (5)$$

The function $\mathcal{E}^0 \mathbf{w} : \Gamma \rightarrow \mathbb{R}^d$ associates, to each point $x \in \Gamma$, the value of \mathbf{w} on the point s on the centerline γ corresponding to the projection $s = \Pi(x)$.

Lemma 1 (Boundedness of extension and average operators). *Under the above assumptions 1 and 2, the average and extension operators*

$$\begin{aligned} \mathcal{A}^0 : \mathcal{Q}_{\Gamma'} &\mapsto \mathcal{W}_{\gamma} \\ \mathcal{E}^0 : \mathcal{W}_{\gamma} &\mapsto \mathcal{Q}_{\Gamma'}. \end{aligned} \tag{6}$$

are linear and bounded.

Proof. The linearity of the operators is a direct consequence of their definitions. The boundedness \mathcal{A}^0 follows from the Schwarz inequality and from the tensor product structure of Γ . The proof for the extension operator \mathcal{E}^0 relies on defining the extension first on the reference cylindrical domain, and then exploiting the properties of the isomorphism between V and the reference cylinder. We refer to [28] for further details. \square

Notice that the function $\mathcal{E}^0 \mathbf{w}$ associates to each set $D(s) = \Pi^{-1}(s)$ the constant value $\mathbf{w}(s)$. The operator \mathcal{E}^0 is thus, by construction, the right inverse of the average \mathcal{A}^0 :

$$\mathcal{A}^0 \mathcal{E}^0 \mathbf{w} = \mathbf{w}. \tag{7}$$

The application of the extension operator after the average operator will be called the *averaged trace operator*:

$$C\mathbf{u} := \mathcal{E}^0 \mathcal{A}^0 \mathcal{T}\mathbf{u} \quad \forall \mathbf{u} \in \mathcal{V}_{\Omega}. \tag{8}$$

Namely, for each \mathbf{u} , the function $C\mathbf{u}$ is constant on the preimages $D(s)$ (for each $s \in \gamma$) and it is equal to the average of the trace of \mathbf{u} over $D(s)$.

Remark 2. *In virtue of (7), the operator $\mathcal{E}^0 \mathcal{A}^0$ is a projection, i.e., it holds*

$$(\mathcal{E}^0 \mathcal{A}^0)^2 \mathbf{q} = \mathcal{E}^0 \mathcal{A}^0 \mathbf{q}, \quad \forall \mathbf{q} \in \mathcal{Q}_{\Gamma'}.$$

The application of operator $\mathcal{E}^0 \mathcal{A}^0$ coincides hence with the projection on the subspace

$$\mathcal{Q}_{\Gamma'_0} := \{ \mathbf{q} \in \mathcal{Q}_{\Gamma'} \mid \mathcal{E}^0 \mathcal{A}^0 \mathbf{q} = \mathbf{q} \} \subset H^{\frac{1}{2}}(\Gamma)^d$$

of constant functions on each section $D(s)$ ($s \in \gamma$).

3 The mixed-dimensional elasticity problem

In the setting introduced in Section 2, we consider the following linear elasticity problem:

$$-\operatorname{div}(\sigma(\mathbf{u})) = \mathbf{f} \quad \text{in } \Omega \setminus V \quad (9a)$$

$$\mathbf{u} = 0 \quad \text{on } \partial\Omega \quad (9b)$$

$$\mathbf{u} - C\mathbf{u} = \mathbf{g} \quad \text{on } \Gamma = \partial V, \quad (9c)$$

where the Cauchy stress tensor σ is the usual linear elasticity tensor defined as

$$\sigma(\mathbf{u}) := \mu \nabla \mathbf{u} + \lambda \operatorname{div} \mathbf{u} \mathbf{I}, \quad (10)$$

and C is the averaged trace operator introduced in (8).

The purpose of the boundary condition (9c) imposed via the operator C is to rigorously introduce the concept of *localized coupling conditions*. Namely, it models a local inflation on the vessel Γ , of Dirichlet nature, that follows the average deformation of the material without “pinning” the boundary of the inclusion to a specific position, thus being not sensitive to variation of the solution on a larger scale.

Remark 3. *This type of boundary condition is used, for example, in the case of mixed materials problems (e.g., water bubble free to move inside a medium) and should not be confused with the type of boundary condition needed for a fixed structure mix material problem (e.g., reinforced concrete).*

We now extend (continuously) the solution \mathbf{u} to the entire domain Ω by considering the auxiliary, fictitious, problem inside V :

$$-\operatorname{div}(\sigma(\mathbf{u})) = \tilde{\mathbf{f}}, \quad \text{in } V, \quad (11)$$

where $\tilde{\mathbf{f}} \in L^2(\Omega)^d$ is an arbitrary extension of \mathbf{f} in the entire Ω and with boundary conditions that impose continuity of \mathbf{u} across Γ .

Testing equations (9a) and (11) with an arbitrary smooth function $\mathbf{v} \in C_c^\infty(\Omega)$, and integrating by parts we obtain a weak form of the extended problem as

$$(\sigma(\mathbf{u}), \nabla(\mathbf{v}))_\Omega + \langle \llbracket \sigma(\mathbf{u}) \rrbracket \cdot \mathbf{n}, \mathbf{v} \rangle_\Gamma = (f, \mathbf{v})_\Omega, \quad \forall \mathbf{v} \in H_0^1(\Omega)^d, \quad (12)$$

where

$$\llbracket \sigma(\mathbf{u}) \rrbracket := \sigma(\mathbf{u})^+ - \sigma(\mathbf{u})^-$$

indicates the jump of $\sigma(\mathbf{u})$ along the outgoing normal direction to $\Gamma = \partial V$.

Such procedure is standard in the literature of fictitious domain methods (see, e.g., [24, 23]), and allows one to efficiently solve Dirichlet problems on complex domains, possibly evolving in time, by embedding them in possibly simpler – fixed – domains.

With little abuse of notation, in what follows we will not distinguish between \mathbf{f} and its extension $\tilde{\mathbf{f}}$.

As next, we rewrite (12) imposing the condition (9c) through a Lagrange multiplier. Namely, we seek $\mathbf{u} \in \mathcal{V}_\Omega$, $\boldsymbol{\lambda} \in \mathcal{Q}_\Gamma$, such that

$$(\sigma(\mathbf{u}), \nabla(\mathbf{v}))_\Omega + \langle (\mathcal{T}^T - C^T)\boldsymbol{\lambda}, \mathbf{v} \rangle_\Gamma = (\mathbf{f}, \mathbf{v})_\Omega, \quad (13a)$$

$$\langle \mathcal{T}\mathbf{u} - C\mathbf{u}, \mathbf{q} \rangle_\Gamma = \langle \mathbf{g}, \mathbf{q} \rangle_\Gamma, \quad (13b)$$

for all $\mathbf{v} \in \mathcal{V}_\Omega$ and $\mathbf{q} \in \mathcal{Q}_\Gamma$.

Let us define the following operators:

$$A : \mathcal{V}_\Omega \rightarrow \mathcal{V}_\Omega' \quad (14)$$

$$\langle A\mathbf{u}, \mathbf{v} \rangle := (\sigma(\mathbf{u}), \nabla(\mathbf{v}))_\Omega \quad \forall \mathbf{u}, \mathbf{v} \in \mathcal{V}_\Omega$$

$$B : \mathcal{V}_\Omega \rightarrow \mathcal{Q}_\Gamma' \quad (15)$$

$$\langle B\mathbf{u}, \mathbf{q} \rangle := \langle (\mathcal{T} - C)\mathbf{u}, \mathbf{q} \rangle_\Gamma \quad \forall \mathbf{u} \in \mathcal{V}_\Omega, \forall \mathbf{q} \in \mathcal{Q}_\Gamma$$

$$B^T : \mathcal{Q}_\Gamma \rightarrow \mathcal{V}_\Omega' \quad (16)$$

$$\langle B^T \mathbf{q}, \mathbf{v} \rangle := \langle \mathbf{q} - (\mathcal{E}^0 \mathcal{A}^0)^T \mathbf{q}, \mathcal{T}\mathbf{v} \rangle_\Gamma \quad \forall \mathbf{v} \in \mathcal{V}_\Omega, \forall \mathbf{q} \in \mathcal{Q}_\Gamma$$

Let us now denote the kernel of B^T as

$$\begin{aligned} \mathcal{Q}_{\Gamma 0} &:= \ker(B^T) = \{ \mathbf{q} \in \mathcal{Q}_\Gamma \mid \langle \mathbf{q} - (\mathcal{E}^0 \mathcal{A}^0)^T \mathbf{q}, \mathcal{T}\mathbf{v} \rangle_\Gamma = 0, \forall \mathbf{v} \in \mathcal{V}_\Omega \} \\ &= \{ \mathbf{q} \in \mathcal{Q}_\Gamma \mid \langle \mathbf{q}, \mathbf{v} \rangle_\Gamma = \langle \mathbf{q}, C\mathbf{v} \rangle_\Gamma, \forall \mathbf{v} \in \mathcal{V}_\Omega \}. \end{aligned} \quad (17)$$

In order for the weak formulation (13) to be well-posed, the space of the Lagrange multipliers shall be restricted to $\mathcal{Q}_\Gamma \setminus \mathcal{Q}_{\Gamma 0}^0$. Using the notations (14), (15), and (16), we thus consider the following problem:

Let $f \in \mathcal{V}_\Omega'$, $g \in \mathcal{Q}_\Gamma'$. Find $u \in \mathcal{V}_\Omega$, $\lambda \in \mathcal{Q}_\Gamma \setminus \mathcal{Q}_{\Gamma 0}^0$ such that

$$\langle A\mathbf{u}, \mathbf{v} \rangle + \langle B^T \boldsymbol{\lambda}, \mathbf{v} \rangle = \langle \mathbf{f}, \mathbf{v} \rangle \quad \forall \mathbf{v} \in \mathcal{V}_\Omega \quad (18a)$$

$$\langle B\mathbf{u}, \mathbf{q} \rangle = \langle \mathbf{g}, \mathbf{q} \rangle \quad \forall \mathbf{q} \in \mathcal{Q}_\Gamma \setminus \mathcal{Q}_{\Gamma 0}^0. \quad (18b)$$

Theorem 1 (Well-posedness). *Let assume that Assumptions 1 and 2 are satisfied. Then, problem (18) admits a unique solution.*

Proof. The operator $A : \mathcal{V}_\Omega \mapsto \mathcal{V}_\Omega'$ is symmetric. From the Poincaré inequality, it follows that it satisfies the infsup condition, i.e., there exists a positive real number $\alpha > 0$ such that

$$\inf_{\mathbf{u} \in \mathcal{V}_\Omega} \sup_{\mathbf{v} \in \mathcal{V}_\Omega} \frac{\langle A\mathbf{u}, \mathbf{v} \rangle}{\|\mathbf{u}\|_{\mathcal{V}_\Omega} \|\mathbf{v}\|_{\mathcal{V}_\Omega}} \geq \alpha > 0. \quad (19)$$

The operator B is bounded, since it the sum of the trace operator, which is linear and bounded [42] and of the operator C which is linear and bounded due to Lemma 1.

Moreover, since B^T is injective on the space $\mathcal{Q}_\Gamma \setminus \mathcal{Q}_\Gamma^0$, it follows that there exists a positive real number $\beta > 0$ such that

$$\inf_{\mathbf{q} \in \mathcal{Q}_\Gamma \setminus \mathcal{Q}_\Gamma^0} \sup_{\mathbf{v} \in \mathcal{V}_\Omega} \frac{\langle B\mathbf{v}, \mathbf{q} \rangle}{\|\mathbf{v}\|_{\mathcal{V}_\Omega} \|\mathbf{q}\|_{\mathcal{Q}_\Gamma}} \geq \beta > 0, \quad (20)$$

therefore B admits a continuous right inverse, and well-posedness of the continuous problem follows from the standard theory of saddle point problems [10]. \square

Corollary 1 (Stresses evaluation). *From the extended problem (12) and from (13), it follows that the Lagrange multiplier satisfies*

$$\langle (\mathcal{T}^T - C^T)\boldsymbol{\lambda}, \mathbf{v} \rangle = \langle \llbracket \sigma \rrbracket \cdot \mathbf{n}, \mathbf{v} \rangle_\Gamma, \quad \forall \mathbf{v} \in \mathcal{V}_\Omega. \quad (21)$$

The relation (21) can be used to recover the solid stresses on the fluid boundary from the Lagrange multiplier.

4 Reduced Lagrange multiplier formulation

In this Section, we apply to problem (18) the reduced Lagrange multiplier framework recently introduced in [28], adapting the original formulation to the case of linear elasticity in \mathbb{R}^d and taking into account the local deformation boundary condition (9c).

The approach is based on constructing a lower-dimensional set of the space of Lagrange multipliers adapted to the geometrical and physical settings of the problem, exploiting the characteristic of how inclusions are defined. The reduction only acts on the boundary condition, the operator B , leaving unchanged the elastic part of the problem.

4.1 Reduced basis functions

Let us consider a set $\Phi^N := \{\varphi_i : \Gamma \rightarrow \mathbb{R}\}_{i \geq 0}^N$, with $\varphi_i \in H^1(\Gamma) \cap C^1(\bar{\Gamma})$, for $i = 1, \dots, N$, and such that, for any $s \in \gamma$,

$$\int_{D(s)} \varphi_i \varphi_j dD(s) = 0, \quad \text{for } i \neq j \quad (22)$$

(φ_i and φ_j are orthogonal with respect to the standard L^2 product in $D(s)$ for $i \neq j$), and

$$\|\varphi_i\|_{L^2(D(s))} = \sqrt{D(s)}. \quad (23)$$

Where $D(s)$ is always to be considered as the preimage of the projection on γ according to (2), and the coordinate s can be omitted.

An example of a set satisfying these condition is given in [28]. Let φ_0 being the constant function equal to 1, which trivially satisfies (23). Following [28], for each $i \geq 0$, we define the weighted average and extension operators

$$\mathcal{A}^i : \mathcal{Q}_{\Gamma'} \rightarrow \mathcal{W}_{\gamma} \quad (24a)$$

$$\mathbf{q} \mapsto \int_D \varphi_i \mathbf{q} \, dD$$

$$\mathcal{E}^i : \mathcal{W}_{\gamma} \rightarrow \mathcal{Q}_{\Gamma'} \quad (24b)$$

$$\mathbf{w} \mapsto \varphi_i \mathbf{w} \circ \Pi.$$

Notice that, for $i = 0$, the definitions (24) are consistent with the definitions (4) and (5), of \mathcal{A}^0 and \mathcal{E}^0 , respectively, given in Section 2. Moreover using density and continuity arguments, the boundedness of \mathcal{E}^0 and \mathcal{A}^0 (Lemma 1) can be extended also to the operators defined in (24), for $i \geq 0$. We refer to [28] and [34, Corollary 2.2] for details.

Using (22) and (23), one obtains a generalization of the property (7), i.e., $\forall \mathbf{w} \in \mathcal{W}_{\gamma}$, it holds

$$\mathcal{A}^i \mathcal{E}^j \mathbf{w} = \int_D \varphi_i \varphi_j \mathbf{w} \circ \Pi \, dD = \mathbf{w} \int_D \varphi_i \varphi_j \, dD = \delta^{ij} \mathbf{w}, \quad (25)$$

where δ^{ij} is the Kronecker delta. Moreover, applying the extension \mathcal{E}^i after the average \mathcal{A}^i , for a given $i \geq 0$, corresponds to the projection on $(\text{Span}\{\varphi_i\})^d$:

$$\mathcal{E}^i \mathcal{A}^i \mathbf{q} \in (\text{Span}\{\varphi_i\})^d \subset \mathcal{Q}_{\Gamma'} \quad \forall \mathbf{q} \in \mathcal{Q}_{\Gamma'}.$$

In particular the space $\text{Span}\{\varphi_0\}$ contains constant functions on each $D(s)$ (for each $s \in \gamma$), i.e.,

$$\text{Span}\{\varphi_0\} = \mathcal{Q}_{\Gamma'}^0 = \{\mathbf{p} \in \mathcal{Q}_{\Gamma'} \mid \mathcal{E}^0 \mathcal{A}^0 \mathbf{p} = \mathbf{p}\}$$

Remark 4. From (25) it follows that, for any $i \geq 0$, the operator \mathcal{A}^i is surjective,

$$\forall \mathbf{w} \in \mathcal{W}_{\gamma}, \exists \mathbf{q}_{\mathbf{w}} := \mathcal{E}^i \mathbf{w} \in \mathcal{Q}_{\Gamma'} \text{ s.t. } \mathcal{A}^i \mathbf{q}_{\mathbf{w}} = \mathbf{w}.$$

Using the reduced basis, the extension, and the average operators introduced in Section 4.1, we aim at defining a reduced formulation of problem (18) via a reduction operator from the *full* space \mathcal{Q}_{Γ} of functions defined on the inclusion boundary, onto a *reduced* space defined on the lower dimensional representative domain γ .

To this purpose, we introduce the transposed operator

$$\begin{aligned} R^T : (\mathcal{W}_{\gamma})^N &\rightarrow \text{Span}\{\phi_1, \dots, \phi_N\} \subset \mathcal{Q}_{\Gamma'} \\ (\mathbf{w}_1, \dots, \mathbf{w}_N) &\mapsto \sum_{i=1}^N \mathcal{E}^i \mathbf{w}_i. \end{aligned} \quad (26)$$

For any $\bar{\mathbf{w}} := (\mathbf{w}_1, \dots, \mathbf{w}_N) \in (\mathcal{W}_\gamma)^N$, $\mathbf{g} \in \mathcal{Q}_\Gamma'$, the duality on Γ is:

$$\begin{aligned} \langle R^T \bar{\mathbf{w}}, \mathbf{g} \rangle_\Gamma &= \int_\Gamma \mathbf{g} \sum_i^N \mathcal{E}^i \mathbf{w}_i \, d\Gamma = \int_\Gamma \mathbf{g} \sum_i^N \varphi_i(\mathbf{w}_i \circ \Pi) \, d\Gamma \\ &= \sum_i^N \int_\Gamma \mathbf{g} \varphi_i(\mathbf{w}_i \circ \Pi) \, d\Gamma = \sum_i^N \int_\gamma \int_D \mathbf{g} \varphi_i(\mathbf{w}_i \circ \Pi) \, dD \, ds \quad (27) \\ &= \sum_i^N \int_\gamma \mathbf{w}_i \int_D \mathbf{g} \varphi_i \, dD \, ds = \sum_i^N \left\langle \mathbf{w}_i, \int_D \mathbf{g} \varphi_i \, dD \right\rangle_\gamma \end{aligned}$$

The reduced formulation of problem (18) can be now written as: given $f \in \mathcal{V}_\Omega'$, $\mathbf{g} \in \mathcal{Q}_\Gamma'$ find $\mathbf{u} \in \mathcal{V}_\Omega$, $\mathbf{\Lambda} \in (\mathcal{W}_\gamma)^N$ such that

$$\langle A\mathbf{u}, \mathbf{v} \rangle + \langle B^T R^T \mathbf{\Lambda}, \mathbf{v} \rangle = \langle f, \mathbf{v} \rangle \quad \forall \mathbf{v} \in \mathcal{V}_\Omega, \quad (28a)$$

$$\langle R B \mathbf{u}, \bar{\mathbf{w}} \rangle = \langle R \mathbf{g}, \bar{\mathbf{w}} \rangle \quad \forall \bar{\mathbf{w}} \in (\mathcal{W}_\gamma)^N. \quad (28b)$$

The terms in (28b) can be defined using (27). In particular, we obtain

$$\langle R B \mathbf{u}, \bar{\mathbf{w}} \rangle_\gamma = \langle B \mathbf{u}, R^T \bar{\mathbf{w}} \rangle_\Gamma = \sum_{i=1}^N \left\langle \mathbf{w}_i, \int_D \boldsymbol{\tau} \mathbf{u} \varphi_i \, dD \right\rangle_\gamma. \quad (29)$$

4.2 Stability analysis

Theorem 1 shows that the full dimensional formulation (18) is well posed only if the space of Lagrange multipliers is properly chosen. As it will be shown in this Section, the advantage of the reduction operator is not only the dimensional reduction, but also the fact that the resulting space can be naturally defined to ensure well-posedness of the resulting formulation.

Lemma 2. *The operator $R^T : (\mathcal{W}_\gamma)^N \rightarrow \text{Span}\{\phi_1, \dots, \phi_N\}$ is injective.*

Proof. The thesis follows from the orthonormality of the functions $\varphi_1, \dots, \varphi_N$ and from the definition of R^T . \square

Lemma 3.

$$\langle R^T \bar{\mathbf{w}}, C \mathbf{v} \rangle_\Gamma = 0 \quad \forall \bar{\mathbf{w}} \in (\mathcal{W}_\gamma)^N, \forall \mathbf{v} \in \mathcal{V}_\Omega \quad (30)$$

Proof. The lemma follows observing that $R^T \bar{\mathbf{w}} \in \text{Span}\{\varphi_1, \dots, \varphi_N\}$ and that $\mathcal{E}^0 \mathcal{A}^0 \boldsymbol{\tau} \mathbf{v} \in \text{Span}\{\varphi_0\}$. \square

Lemma 4. *The operator $(RB)^T$ is injective.*

Proof. Let $\bar{\mathbf{w}} \in (\mathcal{W}_\gamma)^N$ such that $\mathbf{w} \in \ker(B^T R^T)$. It follows that $R^T \bar{\mathbf{w}} \in \ker(B^T)$, i.e. (see Equation (17))

$$\langle R^T \bar{\mathbf{w}}, \mathbf{v} \rangle_\Gamma = \langle R^T \bar{\mathbf{w}}, \mathcal{E}^0 \mathcal{A}^0 \mathcal{T} \mathbf{v} \rangle_\Gamma \quad \forall \mathbf{v} \in \mathcal{V}_\Omega. \quad (31)$$

Since the right hand side in (31) vanishes (Lemma 3) one obtains

$$\langle R^T \bar{\mathbf{w}}, \mathbf{v} \rangle_\Gamma = 0, \quad \forall \mathbf{v} \in \mathcal{V}_\Omega,$$

and hence $R^T \hat{\mathbf{w}} = 0$. From the injectivity of R^T it follows that $\mathbf{w} = 0$. \square

Using the previous results, the next theorem ensures the well-posedness of the reduced formulation.

Theorem 2 (Well-posedness of the reduced problem). *Let assume that the assumptions 1 and 2 are satisfied. Then, the operator $RB : \mathcal{V}_\Omega \mapsto (\mathcal{W}_\gamma')^N$ satisfies the inf-sup condition, i.e., there exists a positive real number $\beta_R > 0$ such that*

$$\inf_{\bar{\mathbf{w}} \in \mathcal{W}_\gamma^N} \sup_{\mathbf{v} \in \mathcal{V}_\Omega} \frac{\langle RB \mathbf{v}, q \rangle}{\|\mathbf{v}\|_{\mathcal{V}_\Omega} \|\bar{\mathbf{w}}\|_{(\mathcal{W}_\gamma)^N}} \geq \beta_R > 0. \quad (32)$$

Proof. Firstly, let us observe that the operator RB , defined in (29), is bounded as it is a combination of trace operator and linear bounded operators.

From assumptions 1 and 2, it follows also that the operator $(RB)^T$ is linear, continuous, and bounded.

Since $(RB)^T$ is also injective (Lemma 4), it follows that RB satisfies an inf-sup condition, and the result follows from standard saddle-point theory [10]. \square

4.3 Axis-symmetric deformation

In this Section, we discuss more in details the case of coupling conditions modeling an axis-symmetric deformation of the vessel wall, i.e., resulting in a source term in (9) of the form

$$\mathbf{g}(x) = g_\gamma \mathbf{n}(x), \quad (33)$$

directed along the normal \mathbf{n} to the interface Γ , where $g_\gamma : \gamma \rightarrow \mathbb{R}^{d-2}$ denotes the inflation or deflation of the vessel (as mentioned in Section 3).

Let us consider a local reference system of cylindrical coordinates $(\rho(s), \theta(s), s)$ along γ , for each point $s \in \gamma$, and let us choose the reduced basis $\hat{\varphi}_i \in \mathcal{Q}_\Gamma$ given by

$$\hat{\varphi}_0(s, \rho(s), \theta(s)) = \sqrt{2} \quad (34)$$

$$\hat{\varphi}_{2k+1}(s, \rho(s), \theta(s)) = \sqrt{2(k+1)\pi^k \rho^n} \cos \theta k, \quad k = 0, 1, \dots \quad (35)$$

$$\hat{\varphi}_{2k+2}(s, \rho(s), \theta(s)) = \sqrt{2(k+1)\pi^k \rho^k} \sin \theta k, \quad k = 0, 1, \dots \quad (36)$$

These functions fulfil assumptions (22) and (23). Moreover, the first two non-constant modes ($k = 1, 2$) correspond to the local coordinates of the normal vector on Γ , i.e.,

$$\mathbf{n}(\mathbf{x}) = \begin{bmatrix} \varphi_1(s, \rho(s), \theta(s)) \\ \varphi_2(s, \rho(s), \theta(s)) \end{bmatrix}, \quad (37)$$

for all $\mathbf{x} \in \Gamma$, and with $s = \Pi(\mathbf{x})$.

Since the source term (33) is directed along the normal to the interface and it depends only on the coordinate on γ , \mathbf{g} can be written as an element of $\text{Span}\{\varphi_1, \varphi_2\}$. In other words, for $\bar{\mathbf{w}} = (\mathbf{w}_1, \mathbf{w}_2, \dots, \mathbf{w}_N) \in (\mathcal{W}_{\gamma})^N$, the right hand side

$$\langle R\mathbf{g}, \bar{\mathbf{w}} \rangle = \langle \mathbf{g}, R^T \bar{\mathbf{w}} \rangle,$$

will only depends on \mathbf{w}_1 and on \mathbf{w}_2 .

From the practical point of view, this observation allows to write the reduced source term in (28b) in the form

$$R\mathbf{g} = \left[\begin{bmatrix} g_\gamma \\ 0 \end{bmatrix}, \begin{bmatrix} 0 \\ g_\gamma \end{bmatrix}, 0, \dots, 0 \right]. \quad (38)$$

Remark 5. Let $\mathbf{q} \in \mathcal{E}^0(\mathcal{W}_\gamma) \subset \mathcal{Q}_{\Gamma'}$ be an axis-symmetric test function whose value depend only on the position on the lower dimensional manifold γ , and let $\mathbf{w} = (w_x, w_y)$ be such that $q = \mathcal{E}^0(\mathbf{w})$. From the definition (28b) one obtains that

$$\langle \mathbf{g}, \mathbf{q} \rangle_\Gamma = \langle R\mathbf{g}, \bar{\mathbf{w}} \rangle$$

where $\bar{\mathbf{w}} = ((w_x, 0), (0, w_y)) \in \mathcal{W}_\gamma^2$.

Hence, a two-dimensional reduced order Lagrange multiplier space (i.e., $N = 2$) is optimal for axis-symmetric problems (as for the case of a normal source), in the sense that axis-symmetric test functions in the original space can be mapped exactly onto reduced ones.

Based upon these observation, in the context of mixed-dimensional modeling, the numerical results in Section 5 will mostly focus on the case $N = 2$. However, it is important to mention that although the normal source is axis-symmetric, this does not hold in general for the displacement solution, for example, in presence of multiple inclusions or general geometries. The numerical test presented in Section 5.3 will focus on the error committed when omitting the extra modes.

5 Numerical results

This section is dedicated to the numerical validation of the reduced Lagrange multiplier approach: three test cases are analysed to attest the stability of the method and

to investigate the role and functioning of the Lagrange multiplier. A fourth example simulates the effective material behaviour.

First we monitor the converge rate of the method on a simplified case where the analytical solution is known, second we compare our immersed version of the boundary condition to the same condition on a domain with physical holes. Third we investigate the role of modes in relation to the accuracy of the method.

The numerical simulations presented in this Section have been obtained using the finite element library deal.II [8]. Visualizations have been created with ParaView [2] (version 5.9).

5.1 Two-dimensional axis-symmetric problem

To validate the numerical method, the first example consists of the special case of a 2D circular domain of radius R , containing a single circular inclusion of radius r_i (with $r_i \ll R$) located at its center. Imposing homogeneous Dirichlet boundary condition on the outer radius and at the inclusion boundary, problem (9) admits an analytical solution of the form [26]

$$u_r = c_2 r + \frac{c_1}{r} \quad \text{with} \quad \begin{cases} c_2 = \frac{-r_i \bar{u}}{R^2 - r_i^2} \\ c_1 = \frac{r_i \bar{u} R^2}{R^2 - r_i^2}, \end{cases} \quad (39)$$

where \bar{u} is the normal Dirichlet data on the inclusion boundary.

The formulation (28) has been solved with piecewise linear finite elements for the displacement and with different values of the dimension N of the reduced Lagrange multipliers space.

An example of numerical solution is depicted in Figure 2, while the convergence study is summarized in Figure 3.

Using a global mesh refinement, we obtain order 0.5 convergence in H^1 and 1.5 in L^2 , as it has to be expected for the immersed method (see [28]). Adaptive local refinement allows to retrieve optimal convergence rates.

5.2 Two-dimensional domain with multiple inclusions

The purpose of the second test is to analyze the results of the model in presence of local interaction of multiple, close, inclusions. In this case, an analytical solution is not available, although the solution found in (39) could be used as an approximation in the proximity of the immersed boundary. Hence, for the validation of the results on the whole domain, we use the numerical solution obtained discretizing the inclusion interface within the computational mesh and imposing a boundary condition in the form

$$\mathbf{u} \cdot \mathbf{n} = \bar{\mathbf{u}} \cdot \mathbf{n} \quad \text{on } \Gamma. \quad (40)$$

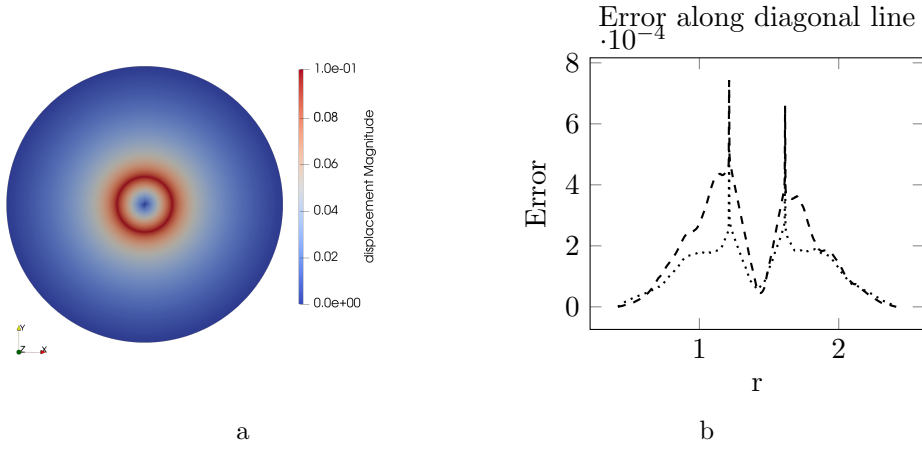


Figure 2: Example 1: Axis-symmetric problem with $R = 1$, $r_i = 0.2$, and $\bar{u} = 0.1$. (a) Numerical solution with $N = 2$. (b) L^2 errors on a cross-section through the lines $y = x$ (dashed) and $y = -x$ (dotted).

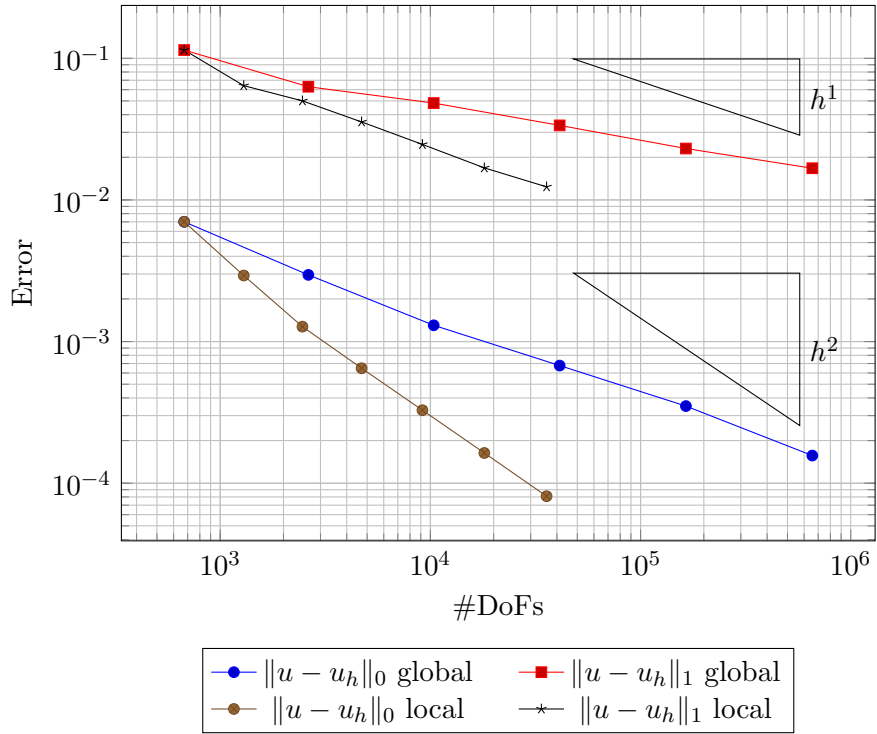


Figure 3: Example 1: Axis-symmetric problem with $R = 1$, $r_i = 0.2$, and $\bar{u} = 0.1$. Convergence rates for the case $N = 2$ with local and global refinements.

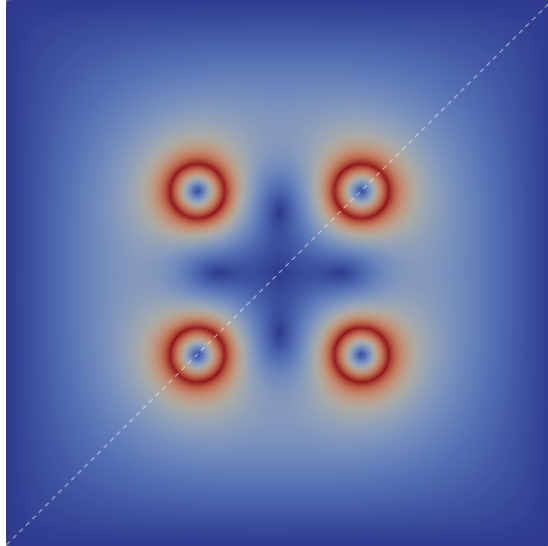


Figure 4: Example 2: Numerical solution (displacement magnitude) for the case of four inclusions: $(0.3, 0.3)$, $(-0.3, 0.3)$, $(0.3, -0.3)$, $(-0.3, -0.3)$, $r_i = 0.1$, $\bar{u} = 0.1$ in the domain $[-1, 1]^2$. The dashed line shows the cross section of the domain used to measure the error in Figure 5.

The condition has been imposed using the non zero flux condition on the boundary Γ provided in [8].

Figure 4 shows the numerical solution obtained with the reduced formulation ($N = 2$) in the case of four inclusions placed symmetrically around the center of a squared domain.

The agreement with the numerical solution in the fully discretized case is confirmed in Figure 5.

5.3 Effect of the higher-order modes

As observed in Section 4.3, imposing a coupling as a normal deformation on the inclusion boundary, whose magnitude only depends on the position along the representative manifold γ , yields a local forcing term that can be naturally written in the 2-dimensional reduced order space (i.e., $N = 2$).

However, in general, the role of modes is subjective to the case analyzed. While $N = 2$ is optimal at the *local* level and it allows, in the single inclusion setting, to obtain the desired rate of convergence, these conclusions cannot be generalized in presence of multiple inclusions, where the overall domain is no longer axis-symmetric, as underlined for the equivalent scalar problem in [28].

Notice that, in this case, the forcing term can no longer be exactly represented in the reduced Lagrange multiplier space of dimension $N = 2$. The purpose of this

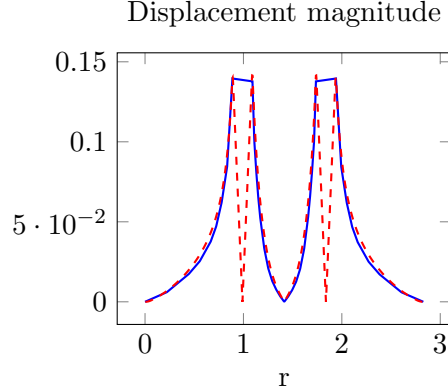


Figure 5: Example 2: Comparison of the displacement magnitudes between the numerical solution with the reduced Lagrange multipliers (red dashed curve) and the corresponding solution obtained discretizing the inclusion boundaries and imposing a non zero flux boundary condition (blue).

example is thus to investigate, the impact of limiting the dimension of the space to $N = 2$. For this purpose, we consider m inclusions located close to each other, and compute the resulting stresses via Equation (21) (i.e., as a function of the reduced Lagrange multipliers) for different geometrical parameters (radii of the inclusions) and dimension N .

Let N be the number of considered modes, which we consider to be the same for each inclusion, and let us denote with $(\mathcal{W}_{\gamma_i}')^N$ the reduced space for the i -th inclusion spanned by N modes. We will then denote with

$$\mathcal{W}_{\gamma'} := \prod_{i=1}^m (\mathcal{W}_{\gamma_i}')^N$$

the space of Lagrange multipliers for all inclusions.

We focus on a two-dimensional spatial setting ($d = 2$). In this case, $\mathcal{W}_{\gamma_i}' = \mathbb{R}^d$ and \mathcal{W}_{γ}' has dimension $m \times (d \times N)$.

In the following discussion, let us denote with

$$\mathbf{\Lambda}^{(j)} = \left[\mathbf{\Lambda}_1^{(j)} \quad \dots \quad \mathbf{\Lambda}_N^{(j)} \right] \in (\mathbb{R}^d)^N$$

the degrees of freedom corresponding to the Lagrange multipliers of the i -th inclusion, and with $\widehat{\mathbf{\Lambda}} = \left[\mathbf{\Lambda}^{(1)}, \dots, \mathbf{\Lambda}^{(M)} \right]$ an element of \mathcal{W}_{γ}' .

The purpose of the numerical example presented in this Section is to assess quantitatively the error

$$\mathbf{\Lambda}^{(2)} = \left[\left[\begin{array}{c} \Lambda_{1,x}^{(2)} \\ 0 \end{array} \right], \left[\begin{array}{c} 0 \\ \Lambda_{2,y}^{(2)} \end{array} \right], 0, \dots, 0 \right],$$

resulting from using only two modes ($N = 2$) on each inclusion, even if the overall problem is no longer axis-symmetric.

The considered numerical example, with $m = 3$, is depicted together with the numerical solution in a particular configuration in Figure 6.

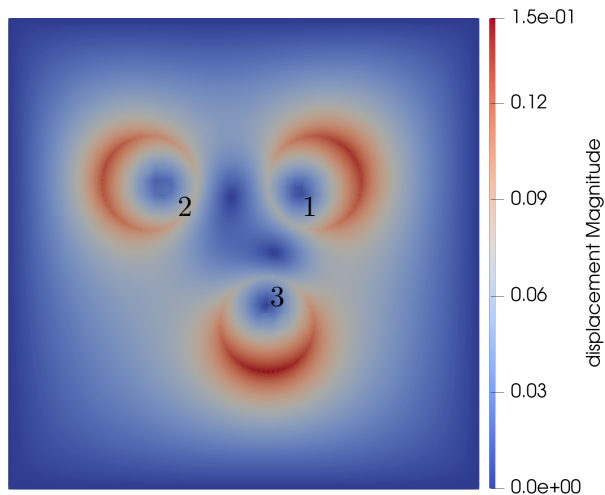


Figure 6: Arrangement and numbering of the inclusions for the analysis of modes at $(0.3, 0.3), (-0.4, 0.3), (0.1, -0.3)$, $r_i = 0.2$, $\bar{u} = 0.1$, in domain $[-1, 1]^2$

Table 1 shows the norm of the Lagrange multiplier solution for the second inclusion ($i = 2$), as a function of the inclusion radius and of the number of modes (up to $N = 8$), comparing the leading order modes (Λ_1 and Λ_2) with the remaining ones. The results for the other inclusions are very similar and will be omitted from the discussion.

The first two components are largely predominant, and the relative truncation error of the order of 10^{-2} (or below). This indicates that $N = 2$ can be used as a suitable approximation also in the non-symmetric case, provided the radii of the inclusions are small enough. Moreover, the truncation error decreases when decreasing the size of the inclusion. This observation is in line with what observed in the context of 3D-1D models coupled via Neumann boundary conditions in [26], in which an hypersingular, axis-symmetric, approximation of the immersed interface was used.

A more detail on the predominance of the leading modes for smaller radii is provided in Figure 7, which depicts, for the second inclusion ($i = 2$) the relative decrease of the higher modes ($N = 4$ to $N = 8$) magnitudes, normalized with respect to the Euclidean

r_i	# Modes	$\ \mathbf{\Lambda}^{(2)}\ _{l_2}$	$\frac{ \Lambda_{1,x}^{(2)} ^2}{\ \mathbf{\Lambda}^{(2)}\ _{l_2}^2}$	$\frac{ \Lambda_{2,y}^{(2)} ^2}{\ \mathbf{\Lambda}^{(2)}\ _{l_2}^2}$	Truncation error (%)
0.2	2	23.91763	54.83%	45.09%	$8.5 \cdot 10^{-2}\%$
0.2	4	23.91763	54.83%	45.09%	$8.5 \cdot 10^{-2}\%$
0.2	6	23.91763	54.83%	45.09%	$8.5 \cdot 10^{-2}\%$
0.2	8	23.91763	54.83%	45.09%	$8.5 \cdot 10^{-2}\%$
0.1	2	88.96162	51.13%	48.87%	$4.01 \cdot 10^{-3}\%$
0.1	4	88.96162	51.13%	48.87%	$4.01 \cdot 10^{-3}\%$
0.1	6	88.96162	51.13%	48.87%	$4.01 \cdot 10^{-3}\%$
0.1	8	88.96162	51.13%	48.87%	$4.01 \cdot 10^{-3}\%$
0.05	2	356.4525	49.98%	50.02%	0%
0.05	4	356.4525	49.98%	50.02%	0%
0.05	6	356.4525	49.98%	50.02%	0%
0.05	8	356.4525	49.98%	50.02%	0%

Table 1: Euclidean l^2 -Norm of the Lagrange multiplier for the second inclusion (number 2 in Figure 6), relative norms of the first two modes, and corresponding relative error for different sizes of inclusions.

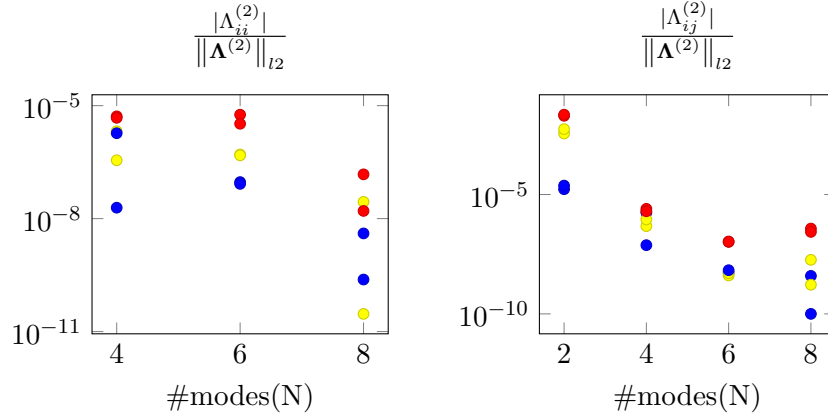


Figure 7: Isotropic components of secondary modes ($\Lambda_{3,x}$, $\Lambda_{4,y}$, $\Lambda_{5,x}$, $\Lambda_{6,y}$, $\Lambda_{7,x}$, $\Lambda_{8,y}$) (left) and anisotropic ($\Lambda_{1,y}$, $\Lambda_{2,x}$, $\Lambda_{3,y}$, $\Lambda_{4,x}$, $\Lambda_{5,y}$, $\Lambda_{6,x}$, $\Lambda_{7,y}$, $\Lambda_{8,x}$) components of lambda and isotropic components of secondary modes (right), for $r_i = 0.2$ (red), 0.1 (yellow), 0.05 (blue)

l^2 norm of $\mathbf{\Lambda}^{(2)}$.

5.4 In-silico modeling of effective material behavior

The proposed multiscale model is motivated by applications in the context of tissue imaging, where the data acquired by techniques such as elastography or diffusion-weighted imaging depend on the underlying physics – e.g., on the interaction of solid and fluid phases – but the limited image resolution allows only for effective (macroscale) tissue representations. Often, these effective descriptions are based on linear elasticity with homogeneous mechanical parameters. However, certain applications require to better understand how the fluid phase, or the structure of the vasculature, are reflected in the behavior of the tissue at the macroscale. This is the case, for instance, of the usage of medical imaging to characterize the presence of pathological conditions in which fluid conditions play a relevant role, such as hypertension (increase in pressure) or tumor growth. To this purpose, it is necessary to develop mathematical models able to close the gap between the microscale (of the underlying physics) and the macroscale (data resolution), and to address related inverse problems for the estimation of effective parameters depending on microscale quantities.

The numerical tests presented in this section are devoted to the usage of the reduced Lagrange multipliers method for the computational modeling and simulation of tissues, investigating the influence of fluid microstructures on tissue effective dynamics. On the one hand, these tests address, from the perspective of mathematical modeling, results recently presented in the context of tissue elastography concerning the importance of understanding the interplay between solid and fluid phases for medical imaging applications in non-invasive diagnostic, see, e.g., [25, 36, 43, 46]. On the other hand, the in silico study aims at providing a first proof of concept for using the reduced Lagrange multipliers in the context of inverse problems for the estimation of effective mechanical parameters.

5.4.1 Effective material parameters for varying microstructure

Setup Firstly, we consider a two dimensional tissue sample with *fixed fluid volume ratio*, but with different distributions of the fluid inclusions. Namely, we consider a fixed number of inclusions with the same radius and three different geometrical setups (see Figure 8):

- (i) inclusions placed in a structured array (denote, in what follows, as *structured*);
- (ii) inclusions placed randomly, but with fixed *microscale* fluid volume ratio, i.e., dividing the domain in boxes, and placing, within each box, an inclusion in a random position (*semi-structured*);
- (iii) inclusions placed fully randomly, but with fixed volume ratio at the *macroscale* (*random*); these configurations have been realized removing overlapping inclusions, and iteratively adding new inclusions until the fixed total number has been reached.

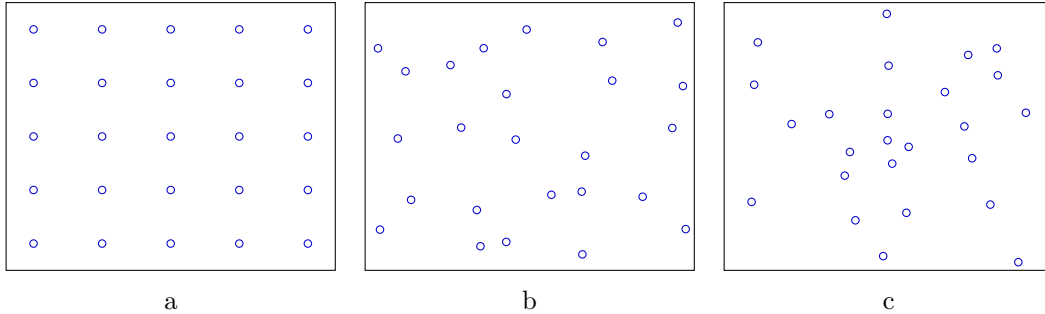


Figure 8: Example of the different setups used for the modeling and simulation of effective material (with $m = 25$ inclusions, $r_i = 0.05$, $v_f \sim 0.05$). Left: inclusions in a structured array. Center: inclusions placed randomly within structured placed boxes (i.e., fixing the porosity in each box). Right: Inclusion placed randomly, removing overlapping ones and fixing the total fluid volume ratio.

In these settings, we study how the behavior of the *effective* material depends on the microstructure, simulating stress and compression tests to compute equivalent mechanical parameters of the effective tissues as functions of the Lamé’s constant λ , μ of the solid matrix, of the boundary condition imposed at the inclusion boundaries (the normal deformation), of the total fluid volume ratio (i.e., of the number of inclusions), and of the vessels distribution.

Compression test The first test is a pure compression (Figure 9, left). The physical domain is the a square $[-1, 1] \times [-1, 1]$, compressed imposing Dirichlet boundary condition on all sides, with a total area reduction of 19%. The material parameters are $\mu = 1$, $\lambda = 1$. The inclusion radius is $r = 0.05$, and, on each inclusion, a normal deformation $\bar{u} = 0.1$ is imposed.



Figure 9: Left: Displacement solution for the compression test (inclusions are not shown). Right: Displacement solution for the shear test. The original configuration is shown in grey in the background.

The effective bulk modulus is computed as the total boundary pressure per area

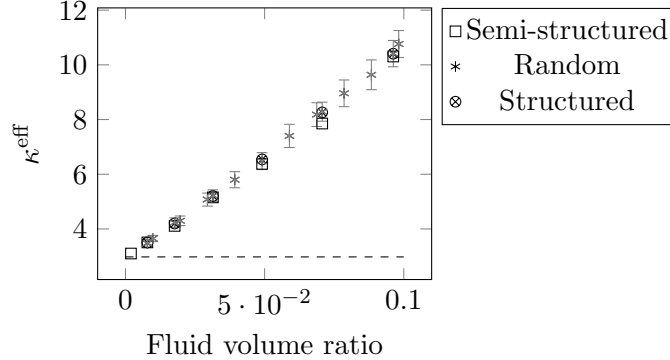


Figure 10: Effective bulk modulus (41) for the compression test, as a function of the fluid volume. The dashed line shows the results for the pure solid case (no inclusions). In the case of random distribution, the picture displays the average and the standard deviation based on $N = 10$ simulations.

difference, i.e.,

$$\kappa^{\text{eff}} = \frac{1}{|\Delta\text{area}|} \frac{1}{|\partial\Omega|} \int_{\partial\Omega} (\sigma(\mathbf{u}) \mathbf{n}) \cdot \mathbf{n}. \quad (41)$$

The results, varying the fluid volume ratio and for different inclusion distributions, are presented in Figure 10. As expected, the presence of the inclusions reduces the compressibility of the effective material, and this effect increases when increasing the fluid volume ratio. In particular, the effective bulk modulus increases by 100% for fluid volume ratio of about 4% and increases by 300% (four times the value of the pure solid matrix) when the fluid volume ratio reaches 10%. We also observe that this effect seems to be independent on the geometrical distribution of the inclusions, i.e., mostly related to the macroscopic volume ratio.

Shear test The second setup (Figure 9, right) considers a material sample with a given horizontal shear rate enforced by Dirichlet boundary condition $\mathbf{u} = (y, 0)$ on the whole boundary. As in the previous example, the physical domain is the square $[-1, 1] \times [-1, 1]$, and the material parameters are $\mu = 1$, $\lambda = 1$. Inclusions have a radius of $r_i = 0.05$ and an imposed normal expansion of $\bar{u} = 0.1$.

In this example, we monitor the effective shear modulus defined as

$$\mu^{\text{eff}} = \frac{1}{2l} \int_{\text{top}} (\sigma(\mathbf{u}) \mathbf{n}) \cdot (1, 0), \quad (42)$$

where $l = 2$ is the edge length.

The results (Figure 11) show that μ^{eff} increases for increasing fluid volume ratio, with an increase up to 50% when the fluid volume ratio reaches 10%. The influence is hence less pronounced with respect to the case of compression. The results are also

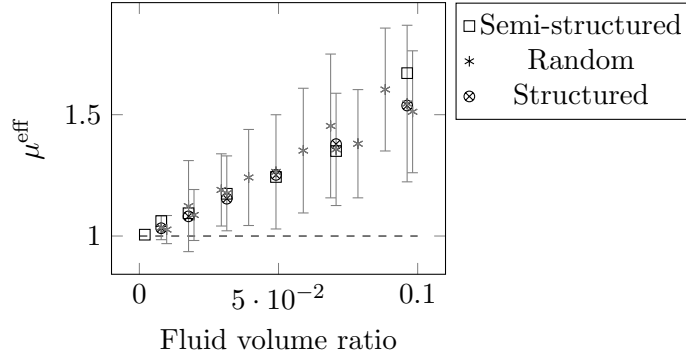


Figure 11: Effective shear modulus (42) for the shear test, varying the fluid inclusion ratio and for different inclusion distributions. The dashed line depicts the results for the pure solid case (without inclusions). The results for the random configuration show the averages and the standard deviations (grey bars) over $N = 10$ simulations.

very similar for the cases of structured and semi-structured inclusion distributions. However, we observe in this case a much higher variability of the results for μ^{eff} in the random setups.

Even if based on a simple two-dimensional setting, these results indicate that the variability of the inclusions structure plays a relevant role in the effective mechanical behavior of the sample and shall not be neglected when aiming at characterizing the response of the multiscale material. The relevance of this effect is expected to considerably grow in three dimensions, also considering additional geometrical parametrizations of the vascular structure (i.e., vessel lengths and directions).

5.4.2 Mechanical response with non uniform fluid structures

The previous examples showed that considering an underlying homogeneous structure for the fluid inclusion results in effective parameters mostly dependent only on the fluid volume ratio. The purpose of the next set of numerical tests is to investigate the influence of non uniform inclusion distributions on the effective mechanical behavior.

To this purpose, we divide the tissue domain in two parts, an inner square and an outer domain, considering structured distributions with a higher density in the inner domain. Namely, the outer domain contains, in all cases, 12 inclusions, while the number of inclusions in the inner domain varies from 9 (3×3) to 121 (11×11). The resulting arrangements are shown in Figure 12. All inclusions have the same radius $r_i = 0.05$ and an expansion in the normal direction of $\bar{u} = 0.01$ is imposed. The elastic properties are set as $\lambda = \mu = 1$.

For each setup (in which the fluid volume ratio and the number of inclusions are fixed), we simulate a compression test and compute the response in terms of tissue pressure on the external boundary for different area reduction.

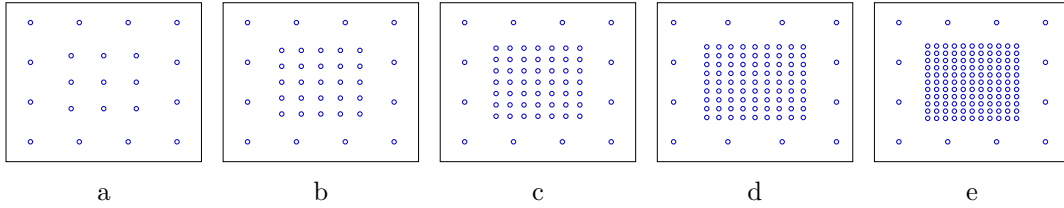


Figure 12: Different setups used for the modeling and simulation of effective material (with $m = 21, 37, 61, 93$ and 133 inclusions, with radius $r_i = 0.05$, corresponding to fluid volume ratios $v_f \sim 0.04, 0.07, 0.12, 0.18, 0.26$).

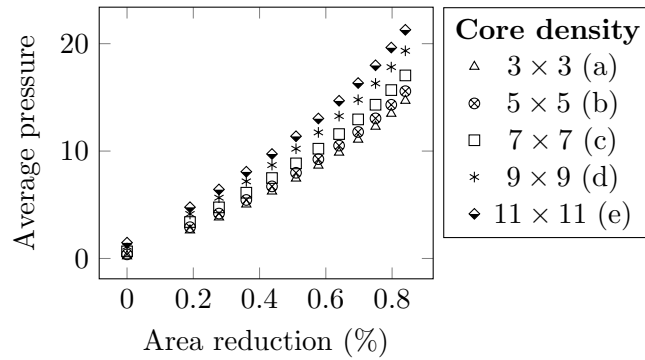


Figure 13: Effective pressure (average on the boundaries) for the compression test in different configurations, as a function of the share of area reduction (starting from an initial area of 4). Notice that also without an external compression, there is a nonzero boundary pressure due to the expansion of the inclusions.

The results in Figure 13 show the presence of a nonlinear mechanical response increasing the compression, highlighting a non trivial interplay between the responses of the inner and outer subdomains. This phenomenon can be observed in all considered samples. Moreover, its effect is more visible when the density contrast between the subdomains increases. This example thus confirms that in presence of complex tissues it is necessary to consider mathematical and computational models that can account for microscale inhomogeneities, in order to correctly represent the effective tissue. As previously observed, it is expected that this effect will be more relevant in three dimensional cases.

6 Conclusions

In this work, we have proposed and investigated an efficient numerical method to simulate multiscale coupled problems involving a linear elastic solid and slender fluid inclusions. The method handles the inclusions as immersed boundaries within the tissue finite element mesh using the reduced Lagrange multiplier approach recently proposed in [28].

In particular, we extended the method of [28] to the case of a *local deformation* boundary condition, in which the fluid and the solid are coupled imposing a local displacement field which does not depend on the macroscale deformation. We showed that this condition can be naturally imposed within the reduced Lagrange multipliers framework by properly selecting the Lagrange multipliers space. In particular, we showed that, with the correct choice of the reduced-order space, the resulting continuous formulation is well-posed.

The immersed method, combined with the reduced Lagrange multiplier approach, allows to reduce the overall complexity of the problem, since the explicit discretization of the inclusion interface is not required. We assessed the performance of the proposed scheme by validating the expected convergence rates in the case of a single inclusion and considering different cases with multiple inclusions. The results show that the proposed multiscale model can be effectively used for the numerical investigation and for the numerical upscaling of multiscale materials. Our tests indicated as well that as the scale separation increases (thinner inclusions), a reduced-order space of dimension $N = 2$ is sufficient for a valid approximation.

Additionally, we performed a detailed study of the influence of microscale quantities (inclusion distribution) on the effective mechanical parameters. The results, although limited to two-dimensional setups, demonstrate that tissue response is sensitive variations and vascular architecture, potentially inducing non-linear mechanical responses in presence of inhomogeneities. These results align with recent discoveries that have emphasized the intricate interconnections between effective parameters at microscales [46].

One natural outlook of this work is the coupling of three-dimensional solid ma-

trices with an active one-dimensional fluid model, generalizing the approach recently proposed in [27]. This extension is currently the subject of ongoing research.

Acknowledgements

The research of C. Belponer has been funded by the Deutsche Forschungsgemeinschaft (DFG, German Research Foundation), grant DFG CA 1159/1-4 and PE 2143/1-6.

L. Heltai acknowledges the partial support of the grant MUR PRIN 2022 No. 2022WKWZA8 "Immersed methods for multiscale and multiphysics problems (IMMEDIATE)"

References

- [1] Assyr Abdulle and Yun Bai. "Reduced basis finite element heterogeneous multiscale method for high-order discretizations of elliptic homogenization problems". In: *Journal of Computational Physics* 231.21 (2012), pp. 7014–7036.
- [2] James Ahrens, Berk Geveci, and Charles Law. "Visualization Handbook". In: Burlington, MA, USA: Elsevier Inc., 2005. Chap. ParaView: An End-User Tool for Large Data Visualization, pp. 717–731.
- [3] Matteo Aletti, Simona Perotto, and Alessandro Veneziani. "HiMod Reduction of Advection-Diffusion-Reaction Problems with General Boundary Conditions". In: *Journal of Scientific Computing* 76.1 (2018), pp. 89–119.
- [4] Robert Altmann, Patrick Henning, and Daniel Peterseim. "Numerical Homogenization beyond Scale Separation". In: *Acta Numerica* 30 (2021), pp. 1–86.
- [5] Robert Altmann and Barbara Verfürth. "A Multiscale Method for Heterogeneous Bulk-Surface Coupling". In: *Multiscale Modeling & Simulation* 19.1 (2021), pp. 374–400.
- [6] Robert Altmann et al. "Computational Multiscale Methods for Linear Heterogeneous Poroelasticity". In: *Journal of Computational Mathematics* 38.1 (2020), pp. 41–57.
- [7] Giovanni Alzetta and Luca Heltai. "Multiscale modeling of fiber reinforced materials via non-matching immersed methods". In: *Computers & Structures* 239 (Oct. 2020), p. 106334.
- [8] Daniel Arndt et al. "The deal.II Library, Version 9.4". In: *Journal of Numerical Mathematics* 30.3 (2022), pp. 231–246.
- [9] Ivo Babuška. "The finite element method with Lagrangian multipliers". In: *Numerische Mathematik* 20 (1973), pp. 179–192.

- [10] Daniele Boffi, Franco Brezzi, Michel Fortin, et al. *Mixed finite element methods and applications*. Vol. 44. Springer, 2013.
- [11] Daniele Boffi and Lucia Gastaldi. “On the existence and the uniqueness of the solution to a fluid-structure interaction problem”. In: *Journal of Differential Equations* 279 (2021), pp. 136–161.
- [12] Daniele Boffi et al. *A parallel solver for fluid structure interaction problems with Lagrange multiplier*. 2022. arXiv: 2212.13410 [math.NA].
- [13] J. H. Bramble. “The Lagrange multiplier method for Dirichlet’s problem”. In: *Mathematics of Computation* 37 (1981), pp. 1–11.
- [14] Donald L. Brown and Daniel Peterseim. “A Multiscale Method for Porous Microstructures”. In: *Multiscale Modeling & Simulation* 14.3 (2016), pp. 1123–1152.
- [15] Ana Budisa et al. “HAZniCS–Software Components for Multiphysics Problems”. In: *arXiv preprint arXiv:2210.13274* (2022).
- [16] Alfonso Caiazzo, Rolf Maier, and Daniel Peterseim. “Reconstruction of Quasi-Local Numerical Effective Models from Low-Resolution Measurements”. In: *Journal of Scientific Computing* 85.10 (2020).
- [17] L. Cattaneo and P. Zunino. “A computational model of drug delivery through microcirculation to compare different tumor treatments”. In: *International Journal for Numerical Methods in Biomedical Engineering* 30.11 (2014), pp. 1347–1371. DOI: 10.1002/cnm.2661.
- [18] L. Cattaneo and P. Zunino. “Computational models for fluid exchange between microcirculation and tissue interstitium”. In: *Networks and Heterogeneous Media* 9.1 (2014), pp. 135–159. DOI: 10.3934/nhm.2014.9.135.
- [19] Carlo D’Angelo and Alfio Quarteroni. “On the Coupling of 1D and 3D Diffusion-Reaction Equations: Application to Tissue Perfusion Problems”. In: *Mathematical Models and Methods in Applied Sciences* 18 (2008), pp. 1481–1504.
- [20] Andrea Franceschini et al. “Algebraically stabilized Lagrange multiplier method for frictional contact mechanics with hydraulically active fractures”. In: *Computer Methods in Applied Mechanics and Engineering* 368 (2020), p. 113161.
- [21] Shubin Fu et al. “Computational Multiscale Methods for Linear Poroelasticity with High Contrast”. In: *Journal of Computational Physics* 395 (2019), pp. 286–297.
- [22] Matteo Gavazzoni et al. “Multi-Physics Inverse Homogenization for the Design of Innovative Cellular Materials: Application to Thermo-Elastic Problems”. In: *Mathematical and Computational Applications* 27.1 (2022).
- [23] Roland Glowinski, Tsorng-Whay Pan, and Jacques Périaux. “A fictitious domain method for Dirichlet problem and applications”. In: *Computer Methods in Applied Mechanics and Engineering* 111 (1994), pp. 283–303.

- [24] Roland Glowinski et al. “A distributed Lagrange multiplier/fictitious domain method for particulate flows”. In: *International Journal of Multiphase Flow* 25 (1999), pp. 755–794.
- [25] J. Guo, I. Sack, and S. Marticorena Garcia. “Liver Magnetic Resonance Elastography: Clinical Use and Interpretation”. In: *Liver Elastography*. Ed. by S. Mueller. Cham: Springer, 2020.
- [26] Luca Heltai and Alfonso Caiazzo. “Multiscale modeling of vascularized tissues via non-matching immersed methods”. In: *International Journal for Numerical Methods in Biomedical Engineering* 35.12 (2019), e3264.
- [27] Luca Heltai, Alfonso Caiazzo, and Lukas O. Müller. “Multiscale Coupling of One-dimensional Vascular Models and Elastic Tissues”. In: *Annals of Biomedical Engineering* 49.12 (2021), pp. 3243–3254.
- [28] Luca Heltai and Paolo Zunino. *Reduced Lagrange multiplier approach for non-matching coupling of mixed-dimensional domains*. 2023. arXiv: 2303.10600 [math.NA].
- [29] Patrick Henning and Daniel Peterseim. “Oversampling for the Multiscale Finite Element Method”. In: *Multiscale Modeling & Simulation* 11.4 (2013), pp. 1149–1175.
- [30] Guillermo H. Jajamovich et al. “Quantitative liver MRI combining phase contrast imaging, elastography, and DWI: assessment of reproducibility and postprandial effect at 3.0 T”. In: *PLoS One* 9.5 (2014), e97355.
- [31] Timo Koch, Hanchuan Wu, and Martin Schneider. “Nonlinear mixed-dimension model for embedded tubular networks with application to root water uptake”. In: *Journal of Computational Physics* 450 (2022), p. 110823.
- [32] M. Kuchta, K.-A. Mardal, and M. Mortensen. “Preconditioning trace coupled 3d-1d systems using fractional Laplacian”. In: *Numerical Methods for Partial Differential Equations* 35.1 (2019), pp. 375–393.
- [33] Miroslav Kuchta et al. “Analysis and Approximation of Mixed-Dimensional PDEs on 3D-1D Domains Coupled with Lagrange Multipliers”. In: *SIAM Journal on Numerical Analysis* 59.1 (2021), pp. 558–582.
- [34] Miroslav Kuchta et al. “Analysis and Approximation of Mixed-Dimensional PDEs on 3D-1D Domains Coupled with Lagrange Multipliers”. In: *SIAM Journal on Numerical Analysis* 59.1 (2021), pp. 558–582.
- [35] Maeva Lewin et al. “Diffusion-weighted magnetic resonance imaging for the assessment of fibrosis in chronic hepatitis C”. In: *Hepatology* 46.3 (2007), pp. 658–665.
- [36] L. Lilaj et al. “Inversion recovery MR elastography of the human brain for improved stiffness quantification near fluid-solid boundaries.” In: *Mag. Res. Med.* 86.5 (2021), pp. 2552–2561.

- [37] Massimiliano Lupo Pasini and Simona Perotto. “Hierarchical model reduction driven by a proper orthogonal decomposition for parametrized advection-diffusion-reaction problems”. In: *ETNA - Electronic Transactions on Numerical Analysis* 55.1 (2021).
- [38] A. Manduca et al. “MR elastography: Principles, guidelines, and terminology”. In: *Magnetic Resonance in Medicine* 85 (2021), pp. 2377–2390.
- [39] Gunda Millonig et al. “Liver stiffness is directly influenced by central venous pressure”. In: *Journal of Hepatology* 52.2 (2010), pp. 206–210.
- [40] Lucas O. Müller et al. “A high-order local time stepping finite volume solver for one-dimensional blood flow simulations: application to the ADAN model”. In: *International Journal for Numerical Methods in Biomedical Engineering* 32.10 (2016), e02761.
- [41] R. Muthupillai et al. “Magnetic resonance elastography by direct visualization of propagating acoustic strain waves”. In: *Science* 269 (1995), pp. 1854–1857.
- [42] John Tinsley Oden. *Applied functional analysis / J. Tinsley Oden, Leszek F. Demkowicz*. eng. CRC series in computational mechanics and applied analysis. Boca Raton: CRC Press, 1996 - 1996. ISBN: 084932551X.
- [43] Naaventhana Palaniyappan et al. “Non-invasive assessment of portal hypertension using quantitative magnetic resonance imaging”. In: *Journal of Hepatology* 65.6 (2016), pp. 1131–1139.
- [44] I. Sack. “Magnetic resonance elastography from fundamental soft-tissue mechanics to diagnostic imaging”. In: *Nature Reviews Physics* 5 (2023), pp. 25–42.
- [45] I. Sack and T. Schöffter, eds. *Quantification of Biophysical Parameters in Medical Imaging*. Springer, 2018.
- [46] Yasmine Safraou et al. “The influence of static portal pressure on liver biophysical properties”. In: *Acta Biomaterialia* (in press).